Research Square

Preprints are preliminary reports that have not undergone peer review.
They should not be considered conclusive, used to inform clinical practice,
or referenced by the media as validated information.

Prediction of p53 Expression in Intrahepatic Mass-forming Cholangiocarcinoma Using a Union Model Based on Intra- and Peritumoral MRI Radiomics

Jiaxuan Tian
Affiliated Hospital of Hebei University
Jinghui Dong
Chinese PLA General Hospital
Guangqian Ren
College of Quality and Technical Supervision, Hebei University
Xiaomeng Li
Hebei University
Lihong Xing
Affiliated Hospital of Hebei University
Liyong Zhuo
Affiliated Hospital of Hebei University
Xueyan Liu
Liaocheng University
Shuo Dai
Liaocheng University
Yanyan Zhang
Beijing YouAn Hospital
Hongjun Li
Beijing YouAn Hospital
Xiaoping Yin
hdfyrad@hbu.edu.cn
Affiliated Hospital of Hebei University
Linyan Xue
College of Quality and Technical Supervision, Hebei University

Research Article

Keywords: Intrahepatic mass-forming cholangiocarcinoma, p53, Magnetic resonance imaging, Radiomics, Peritumoral

Posted Date: April 22nd, 2026

DOI: https://doi.org/10.21203/rs.3.rs-9155751/v1

License: This work is licensed under a Creative Commons Attribution 4.0 International License.
Read Full License

Additional Declarations: No competing interests reported.

Prediction of p53 Expression in Intrahepatic Mass-forming Cholangiocarcinoma Using a Union Model Based on Intra- and Peritumoral MRI Radiomics

Tian Jiaxuan[1,2,3*], Dong Jinghui[6*], Ren Guangqian[4*], Li Xiaomeng[1,2,3], Xing Lihong[1,3], Zhuo Liyong[1,3], Liu Xueyan[5], Dai Shuo[5], Zhang Yanyan[7], Li Hongjun[7], Yin Xiaoping[1,2,3#],Xue Linyan[4#]

1. Department of Radiology, Affiliated Hospital of Hebei University, Baoding, 071000, Hebei Province, People's Republic of China

2. Clinical Medical College, Hebei University, Baoding, 071000, Hebei Province, People's Republic of China

3. Hebei Key Laboratory of Precise Imaging of Inflammation Related Tumors, Baoding, 071000, Hebei Province, People's Republic of China

4. School of Quality and Technical Supervision, Hebei University, Baoding, 071002, Hebei Province, People's Republic of China

5. School of Mathematical Sciences, Liaocheng University, Liaocheng, 252000, Shandong Province, People's Republic of China

6. Radiology Department, the Fifth Medical Center of Chinese PLA General Hospital, Fengtai District, 100039, Beijing, People's Republic of China

7. Department of Radiology, Beijing You'an Hospital, Capital Medical University, Fengtai District, 100039, Beijing, People's Republic of China

***:Tian Jiaxuan, Dong Jinghui and Ren Guangqian contributed equally to this work.**

#:Correspondence to:

Yin Xiaoping: Tel: +86−13103128133

E-mail: hdfyrad@hbu.edu.cn

Xue Linyan: Tel: +18631205753

E-mail: lyxue@hbu.edu.cn

Abstract

Objective: To develop and validate a Union Model integrating clinical features with radiomics signatures derived from intratumoral and peritumoral T2-weighted imaging (T2WI) and diffusion-weighted imaging (DWI) for the non-invasive prediction of p53 expression in intrahepatic mass-forming cholangiocarcinoma (IMCC).Furthermore, the study aims to determine the optimal predictive range.

Methods: This retrospective study included IMCC patients with immunohistochemically confirmed p53 expression status from four institutions. Patients were allocated into training, internal validation, and external validation cohorts. Multi-scale regions of interest, integrating the intratumoral volume with peritumoral expansions of 0, 3, 5, 10, 15, and 20 mm, were delineated on the MRI sequences. Radiomics and clinical features were extracted to construct single-sequence intratumoral and peritumoral models, a Fusion Model, a Clinical

Model, and a Union Model. Performance was assessed using receiver operating characteristic (ROC) curves, area under the curve (AUC), accuracy, sensitivity, and specificity. Model interpretability was explored via SHapley Additive exPlanations (SHAP) values.

Results: The intratumoral and peritumoral 5mm models based on DWI and T2WI sequences demonstrated robust performance, yielding AUCs of 0.959 and 0.987 in the training cohort, and 0.821 and 0.809 in the internal validation cohort, respectively. The Union Model demonstrated the best predictive performance, with AUC values of 0.992, 0.945, and 0.825 across the three cohorts.

Conclusion: A multimodal Union Model incorporating intratumoral and 5-mm peritumoral MRI features can effectively predict p53 expression in IMCC, demonstrating favorable generalizability and potential for clinical decision-making.

Keywords: Intrahepatic mass-forming cholangiocarcinoma; p53; Magnetic resonance imaging; Radiomics; Peritumoral

---

1 Introduction

Intrahepatic mass-forming cholangiocarcinoma (IMCC), a malignancy originating from the bile duct epithelium, accounts for approximately 40% of all intrahepatic cholangiocarcinoma (ICC) cases. Its incidence has been rising rapidly in recent

years[1]. Owing to the insidious nature of early clinical symptoms, only 12%-40% of patients are eligible for surgical resection at the time of diagnosis. Furthermore, ICC is associated with a poor prognosis, characterized by a 5-year survival rate of 25%-40% and a high recurrence risk ranging from 50% to 70%[2]. For patients with advanced local metastasis or postoperative recurrence, the efficacy of various adjuvant therapies remains under clinical exploration[3].Consequently, predicting the expression of tumor microenvironment-related biomarkers in ICC is critical for prognosis monitoring and treatment strategy adjustment[4,5]. Previous studies have found that positive p53 expression is an independent predictor of poor prognosis in colorectal cancer[6]. Missense mutations in the *TP53* gene result in the high expression of p53 protein, making its monitoring indicative of patient prognosis. While ICC is frequently initially detected via imaging, IMCC is confirmed pathologically. Therefore, combining imaging features with clinicopathological information to construct a predictive model holds great potential for the early diagnosis and therapeutic management of IMCC patients.

The *TP53* gene, identified as one of the most prevalent driver gene mutations in the development of IMCC, is categorized into wild-type and mutant types[7]. Wild-type *TP53* serves as a vital tumor suppressor gene, and its encoded p53 protein plays a central role in maintaining DNA stability and normal cellular physiological metabolism[8]. Mutant *TP53* may promote tumor cell invasion and migration, potentially contributing to the aggressiveness, drug resistance, and poor prognosis of ICC[9]. When *TP53* undergoes a missense mutation, the resulting accumulation of p53

protein not only leads to the loss of its inherent tumor-suppressive function but also the acquisition of oncogenic properties, thereby posing a risk to patient prognosis[10,11]. A p53 protein positivity rate exceeding 70% strongly suggests the presence of a *TP53* gene mutation[6,12]. Given the limitations of gene sequencing technology, the development of a preoperative predictive model for p53 protein expression status holds significant research value for precise, non-invasive screening within the immunomolecular field for IMCC patients.

Radiomics extracts and decodes high-throughput imaging features most relevant to biomarkers to construct reliable predictive models[13,14], and has been widely applied in preoperative diagnosis, postoperative follow-up, and early non-invasive risk assessment of ICC[15,16].Among imaging modalities, MRI, with its superior soft-tissue resolution, is utilized to predict the biological behavior and prognosis of ICC. For instance, a high signal on DWI suggests higher tumor cellular density and a poorer prognosis[17] ; meanwhile, the "target sign" on T2WI sequences offers advantages in identifying poorly differentiated IMCC[18].In studies developing machine learning models to predict *TP53* mutations in intramedullary glioma and cervical cancer, radiomics models have demonstrated favorable predictive performance[19,20]. However, no MRI-based radiomics model currently exists for the risk assessment and grading of p53 expression status in IMCC. Moreover, research focusing on peritumoral regions has been limited to specific expansion ranges[21], lacking a systematic comparison to determine the optimal predictive range and a rigorous methodology. Therefore, this study aims to utilize machine learning methods to construct radiomics models based

on the optimal intratumoral and peritumoral prediction ranges, and further integrate these with clinical and imaging features to establish a multimodal Union Model for predicting p53 protein expression status, thereby offering a new perspective for ICC prognosis assessment.

2 Materials and Methods

2.1 Study Population

A total of 312 patients with pathologically confirmed IMCC were initially identified from four medical centers. Following the application of inclusion and exclusion criteria, 104 patients were finally enrolled in this study. Data from three centers were randomly split in an 8:2 ratio into an internal training cohort (n=61) and an internal validation cohort (n=16). Data from the remaining independent center served as the external validation cohort (n=27).Inclusion criteria included the following: 1) underwent curative liver resection; 2) resected lesion pathologically diagnosed as IMCC, with p53 expression status assessed by immunohistochemistry (IHC); 3) underwent preoperative non-contrast MRI within 2 weeks before surgery; 4) maximum lesion diameter ≥ 10 mm, allowing successful delineation of peritumoral regions; 5) patient age ≥ 18 and ≤ 75 years. Exclusion criteria included the following: 1) missing preoperative imaging data or poor image quality preventing evaluation; and 2) a history of other malignancies, presence of distant metastasis, or preoperative radiotherapy/chemotherapy.The patient selection flowchart is shown in Figure 1.

2.2 Examination Methods

MRI examinations across the four research centers were conducted using either 1.5-T or 3.0-T MRI scanners, including the Siemens Amira 1.5-T, Philips Achieva 1.5-T, United Imaging, and GE Discovery 750 3.0-T, for axial upper abdominal scanning. Detailed scanning parameters for each sequence are provided in Supplementary Material 1.

2.3 Clinical and Imaging Feature Analysis

Imaging features were qualitatively assessed by two radiologists. Any discrepancies in their evaluations were resolved through discussion to reach a consensus. The evaluated imaging features encompassed:(a) Lesion location: involving left lobe, right lobe, or both; (b) Tumor morphology: regular (clear transition between lesion and adjacent liver parenchyma) or irregular; (c) T2WI tumor margin: clear (sharp boundary) or indistinct; (d) Perilesional bile duct dilation; (e) Liver capsule retraction: retraction or unevenness of the liver capsule adjacent to the lesion; (f) Intrahepatic bile duct stones; (g) Vascular involvement: involvement of the main trunk or branches of the portal vein, hepatic vein, or hepatic artery; (h) Vessel penetration sign: branches of hepatic, portal veins, or hepatic artery traversing the lesion; (i) Enlarged lymph nodes: short-axis diameter ≥1.0 cm; (j) T2WI signal pattern: overall isointense, homogeneously hyperintense, heterogeneously hyperintense, peripheral hyperintensity with internal hypointensity, peripheral hypointensity with internal hyperintensity, or hypointense; (k) DWI signal pattern[24,25]: overall isointense,

homogeneously hyperintense, heterogeneously hyperintense, peripheral hyperintensity with internal hypointensity, peripheral hypointensity with internal hyperintensity, or hypointense.

Clinical features included: sex, age, Alpha-fetoprotein(AFP), Carbohydrate antigen 125(CA125), Carbohydrate antigen 19-9(CA19-9), Carcinoembryonic antigen(CEA), and p53 protein expression status. In clinical practice, p53 protein positivity was defined as nuclear staining in >70% of tumor cells[12]; otherwise, it was considered negative.

2.4 MRI Image Segmentation and Preprocessing

Original DWI and T2WI sequence images were retrieved in DICOM format from the Picture Archiving and Communication System (PACS). Image segmentation was initially conducted using 3D Slicer software. To assess inter-observer reliability, all patient segmentations were performed by a radiologist with 5 years of experience in abdominal imaging diagnosis, while a second radiologist with 10 years of experience independently segmented images from 30 randomly selected patients.While blinded to clinical data, the radiologists utilized ITK-SNAP software (version 3.8.0) to manually delineate the tumor on a slice-by-slice basis, thereby defining the intratumoral region of interest (ROI). Utilizing the cv2.getStructuringElement function from the Python OpenCV library (version 4.8.0), the tumor boundaries were radially expanded by 0, 3, 5, 10, 15, and 20 mm. This process defined composite regions of interest encompassing both the intratumoral and peritumoral volumes, with the 0 mm margin

representing the original intratumoral volume.Any segmentations extending beyond the liver parenchyma were manually adjusted for accuracy. Consequently, for each sequence, one intratumoral (0 mm) and five peritumoral ROIs were generated: Peri-0mm, Peri-3mm, Peri-5mm, Peri-10mm, Peri-15mm, and Peri-20mm. Prior to feature extraction, the original images underwent Z-score normalization for grayscale normalization to enhance feature robustness.

2.5 Optimal Machine Learning Algorithm

Seven machine learning classifier algorithms were employed: Logistic Regression (LR), Support Vector Machine (SVM), K-Nearest Neighbor (KNN), Random Forest (RF), Bayesian, Extreme Gradient Boosting (XGBoost), and Light Gradient Boosting Machine (LightGBM). Models were constructed based on the intratumoral ROI and comparatively evaluated to identify the optimal algorithm for subsequent analyses.

2.6 Feature Extraction and Selection

Radiomics feature extraction was conducted using Python (version 3.8.20) with the following libraries: numpy (1.24.4), Pandas (1.5.3), SimpleITK (2.3.0), nibabel (5.2.1), Radiomics (v3.0.1), and tqdm (4.67.1), resulting in a total of 6,539 extracted features. The preliminary feature selection process followed a systematic workflow:1) low-variance filtering: Uninformative features with a variance < 0.005 were removed; 2) High-correlation filtering: Redundant features with a Pearson correlation coefficient > 0.98 were excluded; and 3) Statistical test filtering: Significant features

were selected using the ANOVA F-test (p-value<0.08), with only those scoring above the first quartile being retained.Finally, by integrating Random Forest (RF) feature importance with ANOVA scores, the 11 most significant radiomics features were retained for model construction.

To evaluate the reproducibility of the extracted radiomics features, the Intraclass Correlation Coefficient (ICC) was utilized to assess both intra- and inter-observer stability for the intratumoral and peritumoral regions. Only features demonstrating high stability, defined by an ICC ≥ 0.85 , were retained for subsequent analyses.

Regarding clinical and imaging features, the SelectFromModel method was utilized to extract features with importance scores exceeding the mean value derived from a trained Random Forest (RF) model. The selected features were subsequently standardized and utilized for downstream model training, ensuring that only the most discriminatory features for predicting p53-positive/negative status were retained.

2.7 Model Construction

Based on the optimal machine learning algorithm identified, 12 single-sequence radiomics models were constructed using the six ROIs derived from both DWI and T2WI sequences. From these, the best-performing model for each respective sequence was selected. These two optimal single-sequence models were then integrated to establish the Fusion Model. Concurrently, the selected clinical and imaging features

were utilized to construct the Clinical Model. Finally, the Fusion Model and the Clinical Model were integrated to form the Union Model.

2.8 Statistical Analysis and Model Evaluation

Statistical analysis was performed using SPSS 24.0 and Python (v.3.8.5). Baseline continuous variables are presented as the mean ± standard deviation and categorical variables as frequency and percentage. Levene's test was used to assess homogeneity of variance between groups. For continuous variables with homogeneous variance, the independent samples t-test was used; for categorical variables, the chi-square test or Fisher's exact test was used. A P-value < 0.05 was considered statistically significant for differences between groups.

Model performance was evaluated by plotting receiver operating characteristic (ROC) curves and calculating the area under the curve (AUC), accuracy, sensitivity, and specificity. Predictive performance was assessed using confusion matrices. The external validation cohort was used to test model generalizability. SHapley Additive exPlanations (SHAP) analysis was employed for model interpretability, explaining feature contributions.

3 Results

3.1 General Clinical Data

Based on the predefined inclusion and exclusion criteria, 104 IMCC patients were enrolled in this study. The cohort consisted of 79 patients with p53-positive expression and 25 with p53-negative expression. For model development and evaluation, the patients were stratified into a training cohort of 61 cases, an internal validation cohort of 16 cases, and an independent external validation cohort of 27 cases. Detailed baseline clinical characteristics are summarized in Table 1. No significant difference in characteristics was found among the different groups.

3.2 Optimal Machine Learning Method

The predictive performance of intratumoral radiomics models, constructed using seven distinct machine learning algorithms, was comprehensively evaluated, with the corresponding ROC curves illustrated in Figure 2. While multiple methods demonstrated high diagnostic efficacy within the training cohort, the Random Forest model yielded the most superior and stable results upon evaluation in the internal validation cohort. Consequently, the Random Forest algorithm was selected as the optimal modeling approach for this study, as it exhibited an ideal balance between high accuracy and robust generalizability across the two cohorts.

3.3 Clinical, Imaging, and Radiomics Features

Using the clinical feature selection method, six clinical/imaging features were finally included in the clinical model: age, AFP, CEA, T2WI tumor margin, CA19-9, and liver capsule retraction.

From a total of 6,539 raw radiomic features extracted from the DWI and T2WI sequences, 11 core features were identified through a rigorous selection process. Among these, six originated from the DWI sequence and five from the T2WI sequence. The final feature set comprised seven features based on Laplacian of Gaussian (LoG) filters, three derived from wavelet transforms, and one based on a square transform.

3.4 Performance Comparison of Single-Sequence Intratumoral and Peritumoral Models on DWI/T2WI

ROC curves for the 12 single-sequence radiomics models in the training and internal validation cohorts are shown in Figure 3. For detailed comparison, the AUC, sensitivity, accuracy, and specificity results of these 12 models are summarized in Table 2. All single-sequence intratumoral and peritumoral radiomics models showed certain predictive values. DeLong's test indicated no statistically significant difference in AUC among the single-sequence models. Therefore, by comparing AUC differences and model robustness, the optimal prediction range models were selected. The results showed that the intratumoral and peritumoral 5 mm models on DWI and T2WI sequences (PeriD-5mm and PeriT-5mm) had the best predictive performance. In the internal training and validation cohorts, the PeriD-5mm model had AUC values of 0.959 (95% CI: 0.958–0.960) and 0.821 (95% CI: 0.812–0.831), respectively. The PeriT-5mm model had AUC values of 0.987 (95% CI: 0.986–0.987) and 0.809 (95% CI: 0.802–0.817), respectively.

3.5 Performance Comparison and Evaluation of the Union Model, fuision Model, and Clinical Model

3.5.1 ROC curves for the Union Model, Fusion Model, and Clinical Model in the training, internal validation, and external validation cohorts are shown in Figure 4. The Union Model outperformed the Fusion Model and the Clinical Model. The AUC, sensitivity, accuracy, and specificity of the three models are shown in Table 3. The Fusion Model, formed by merging the PeriD-5mm and PeriT-5mm models, showed improved overall predictive performance compared to single-sequence models, with AUC values of 0.933 (95% CI: 0.932–0.935), 0.945 (95% CI: 0.941–0.949), and 0.777 (95% CI: 0.771–0.784) in the three cohorts, respectively. The Union Model demonstrated the best predictive efficacy across the three cohorts, with AUC values of 0.992 (95% CI: 0.992–0.993), 0.945 (95% CI: 0.941–0.949), and 0.825 (95% CI: 0.819–0.831), respectively. The Clinical Model had AUC values of 0.864 (95% CI: 0.754–0.953), 0.718 (95% CI: 0.429–0.974), and 0.650 (95% CI: 0.382–0.892), respectively. The addition of clinical features increased the Union Model's AUC by 0.05–0.10 compared to the Fusion Model across cohorts and improved model robustness, indicating the contribution of clinical/imaging factors.

3.5.2 The confusion matrices for the Fusion, Clinical, and Union models across the training, internal validation, and external validation cohorts are illustrated in Figure 5. Among these, the Union Model demonstrated the most superior accuracy in differentiating between p53-negative and p53-positive expression across all three cohorts. Furthermore, this model exhibited the highest level of concordance between

predicted outcomes and actual pathological results, alongside the most robust generalizability. Specifically, the accuracy rates for predicting p53-negative versus p53-positive status within the three cohorts were 96.8% vs. 93.3%, 66.7% vs. 92.3%, and 85.7% vs. 75.0%, respectively.

3.5.3 To further elucidate the decision-making logic of the ensemble model, SHAP analysis was performed on the features used to predict p53-positive expression. As illustrated in Figure 6, the SHAP summary plot ranks features by their relative importance, where higher positions indicate a greater contribution to the model's output. The distribution of SHAP values reveals the directional influence of each feature. A positive SHAP value indicates a tendency to predict p53 positivity, whereas a negative value suggests a predication toward negativity.Each point on the plot represents an individual sample, with red indicating high feature values and blue indicating low feature values. Higher SHAP values signify a stronger association with p53-positive expression, while lower values correlate more closely with negativity. The SHAP analysis identifies the top five predictors as radiomic features derived from the combined intratumoral and peritumoral regions of both DWI and T2WI sequences. These core features include two obtained via wavelet transformation and three via Laplacian of Gaussian filtering. These findings confirm the significant predictive value of integrated intratumoral and peritumoral information in characterizing p53 status.

3.5.4 The original images of IMCC patients with p53-negative and p53-positive expression are presented in Figure 7. In p53-negative patients, both DWI and T2WI sequences showed central hypointensity with peripheral hyperintensity, whereas in p53-positive patients, the signal was homogeneously hyperintense, with even higher signal intensity centrally on T2WI.

4 Discussion

4.1 This study systematically evaluated the predictive value of various combined intratumoral and peritumoral regions—extending 3, 5, 10, 15, and 20 mm from the tumor boundary—to characterize p53 expression status in IMCC. Our findings identified the 5-mm expansion as the optimal predictive range. Building upon this, the Union Model was developed by integrating these multi-scale radiomic features with clinical factors. This comprehensive approach demonstrated superior diagnostic efficacy and robust generalizability across both the training and validation cohorts.

The p53 protein represented a pivotal biomolecular marker for the routine diagnosis and differential identification of intrahepatic cholangiocarcinoma (ICC)[24], with intrahepatic mass-forming cholangiocarcinoma (IMCC) being its most prevalent histological subtype[25]. While recent research predominantly focused on therapeutic strategies to inhibit IMCC progression via the p53 signaling pathway[26], the inherent limitations of immunohistochemical (IHC) analysis—specifically its invasive nature and inability to provide a comprehensive assessment of tumor invasiveness—were frequently overlooked. Consequently, this study was dedicated to developing

non-invasive radiomics-based tools to facilitate early p53 screening and enable the longitudinal monitoring of therapeutic efficacy.

Dynamic alterations in biomolecular markers within the peritumoral region significantly influenced tumor progression. Fiz et al. [27] developed a CT-based radiomics model integrating both intratumoral and peritumoral regions within a 5-mm margin, enabling precise preoperative prognostic prediction for ICC. Additionally, Pan et al. [28] constructed a Union Model for predicting lymph node metastasis, confirming that peritumoral information substantially enhanced predictive efficacy. While these studies validated the clinical utility of peritumoral regions, their models were limited to a single fixed expansion, lacking a standardized and systematic comparison across various peritumoral zones—an aspect that the present study sought to refine.

Xu et al. [29] suggested that radiomics models integrating both intratumoral and peritumoral 5-mm regions were more effective for predicting early ICC recurrence, as they captured critical information regarding satellite nodules and microvascular invasion (MVI). Their finding that the 5-mm margin outperformed the 3-mm margin was consistent with our results, which also identified 5 mm as the optimal predictive range. Conversely, we observed that larger peritumoral regions exhibited unstable predictive performance. We hypothesized that as the peritumoral expansion increased, increasingly active molecular interactions within the tumor-immune microenvironment (TIME) might have interfered with the representation of p53

expression, thereby diminishing predictive efficacy. This was consistent with Huang et al. [30], who noted that excessively large margins incorporated a higher proportion of normal hepatic parenchyma, which effectively diluted the p53-related radiomic signals. Consequently, the combined intratumoral and peritumoral 5-mm regions achieved an ideal balance between information density and specificity; they sufficiently covered the tumor-immune interface while minimizing the inclusion of normal liver tissue, thereby ensuring robust and stable model performance.

In the training cohort, models based on T2WI sequences outperformed those using DWI for the combined intratumoral and peritumoral 5-mm regions. This superiority likely stemmed from the enhanced capacity of T2WI to resolve tumor morphology and textural heterogeneity compared with other sequences. Conversely, DWI sequences yielded higher model stability overall, suggesting that information regarding cellular density and diffusion restriction reflected by DWI correlated more closely with p53 expression status. While the Fusion Model demonstrated improved performance over single-sequence models only in the internal validation cohort, Xu et al.[31] found that a multiparametric approach integrating T2WI and DWI consistently outperformed single-sequence configurations. This discrepancy might have been attributed to the relatively limited sample size in the present study, which likely contributed to a degree of overfitting in the training cohort.

Although the clinical features incorporated into the Clinical Model did not reach statistical significance in this specific cohort, their established associations with p53

and prognosis maintained considerable clinical utility. For instance, elevated levels of CA19-9 and CEA were recognized as indicators of increased recurrence risk and poor prognosis in IMCC patients [29]. Furthermore, Ji et al. [32] identified liver capsule retraction as a significant correlate of adverse outcomes in IMCC. Additionally, parameters such as AFP levels and T2WI-defined tumor margins remained highly effective for the differential diagnosis between hepatocellular carcinoma and ICC [33]. The integration of these variables into our Union Model aimed to leverage their known biological relevance to enhance overall model robustness.

The top five texture features identified by the Union Model for predicting p53-positive expression were all derived from the combined intratumoral and peritumoral 5-mm regions of the DWI and T2WI sequences. Notably, DWI sequences exhibited a stronger intrinsic association with p53 positivity. This was consistent with the findings of Qian et al. [34], whose model for predicting Ki-67 status in ICC also assigned greater predictive weight to DWI-derived features.The dominance of DWI likely reflected its sensitivity to alterations in cellular density and membrane integrity. Specifically, as tumor cell proliferation intensified, heightened structural complexity and diffusion restriction led to decreased ADC values, which collectively signified elevated p53 expression. Simultaneously, texture features from T2WI sequences captured essential aspects of tumor heterogeneity. Higher T2WI signal intensity often correlated with increased textural complexity, which further reflected the aggressive biological behavior associated with p53 overexpression, a relationship previously validated by Wang et al. [35].

4.2 Limitations

Firstly, this retrospective study was performed on a relatively small sample size, which may have led to bias and potential overfitting of model parameters in the internal training cohort. Secondly, the study did not include a prospective cohort, so incorporating prospective data would enhance model interpretability and validity. Thirdly, this study extracted radiomics features only from high-resolution T2WI and DWI sequences, which provided limited information. Future research should extract features from contrast-enhanced MRI, molecular imaging, etc., to build more comprehensive and stable models. Finally, incorporating *TP53* gene sequencing results as a reference for comparison with the Union Model's predictions could further validate its predictive performance.

5 Conclusion

The Union Model constructed based on intratumoral and peritumoral 5 mm MRI radiomics features and clinical features effectively predicted p53 expression status in IMCC, demonstrating certain generalizability and clinical potential. This aided in promoting precise diagnosis and treatment for IMCC, potentially improving patient prognosis. The optimal prediction range was intratumoral and peritumoral 5 mm.

Abbreviations

AFP: Alpha-fetoprotein

CA125: Carbohydrate antigen 125

CA19-9: Carbohydrate antigen 19-9

CEA: Carcinoembryonic antigen

ICC: Intrahepatic cholangiocarcinoma

IHC: Immunohistochemistry

IMCC: Intrahepatic mass-forming cholangiocarcinoma

DWI: Diffusion-weighted imaging

GLCM: Gray level co-occurrence matrix

GLDM: Gray level dependence matrix

GLRLM: Gray level run length matrix

GLSZM: Gray level size zone matrix

MRI: Magnetic resonance imaging

NGTDM: Neighboring gray tone difference matrix)

ROI: Region of interest

T2WI: T2-weighted imaging

AUC: Area under the curve

CI: Confidence interval

KNN: K-nearest neighbor

LightGBM: Light gradient boosting machine

LR: Logistic regression

RF: Random forest

ROC: Receiver operating characteristic

SHAP: SHapley Additive exPlanations

SVM: Support vector machine

XGBoost: Extreme gradient boosting

Declarations

Author Contributions

Tian Jiaxuan and Dong Jinghui contributed equally to this work. They contributed substantially to the study by performing literature search, designing the study, collecting and analyzing data, and drafting the manuscript. Ren Guangqian and Li Xiaomeng focused on model construction and figure preparation. Xing Lihong, Zhuo Liyong, Liu Xueyan, Dai Shuo, Zhang Yanyan, and Li Hongjun were involved in data collection and interpretation. Yin Xiaoping and Xue Linyan assisted in data interpretation. All authors critically reviewed, revised, and approved the final manuscript.

Data availability statement

The data that support the findings of this study are available from the corresponding author upon reasonable request.

Funding

This work was supported by the 2026 Government-funded Program for the Training of Excellent Clinical Medical Personnel （ZF2026438).

Ethical approval

The study retrospectively collected data from four centers, including the Affiliated Hospital of Hebei University, Beijing Youan Hospital, Capital Medical University, the Fifth Medical Center of the Chinese People's Liberation Army General Hospital, and Shandong Provincial Hospital Affiliated to Shandong First Medical University. This study was approved by the Ethics Committees of the respective hospitals (Approval Numbers: HDFYLL-IIT-205-121, LL-2021-019-K, KY2024-12-196-1, and SWYX: NO. 2025-160), and the requirement for informed consent was waived in accordance with the guidelines of the Council for International Organizations of Medical Sciences (CIOMS).

Consent for publication

Consent for publication is Not Applicable.

Competing interests

The authors have no conflicts of interest to declare.

Acknowledgements

We gratefully acknowledge the aforementioned hospitals and clinical departments for their essential data support and cooperation.

References

[1] Qurashi M, Vithayathil M, Khan SA. Epidemiology of cholangiocarcinoma. Eur J Surg Oncol. 2025;51(2):107064. doi: 10.1016/j.ejso.2023.107064.

[2] Moris D, Palta M, Kim C, et al. Advances in the treatment of intrahepatic cholangiocarcinoma: An overview of the current and future therapeutic landscape for clinicians. CA Cancer J Clin. 2023;73(2):198-222. doi: 10.3322/caac.21759.

[3] Gravely A, Vibert E, Sapisochin G. Surgical treatment of intrahepatic cholangiocarcinoma. J Hepatol. 2022;77(3):865-867. doi: 10.1016/j.jhep.2022.01.004.

[4] Banales JM, Marin JJG, Lamarca A, et al. Cholangiocarcinoma 2020: the next horizon in mechanisms and management. Nat Rev Gastroenterol Hepatol. 2020;17(9):557-588. doi: 10.1038/s41575-020-0310-z.

[5] Andraus W, Tustumi F, de Meira Junior JD, et al. Molecular profile of intrahepatic cholangiocarcinoma. Int J Mol Sci. 2023;25(1):461. doi: 10.3390/ijms25010461.

[6] Kim KM, Ahn AR, Park HS, et al. Clinical significance of p53 protein expression and *TP53* variation status in colorectal cancer. BMC Cancer. 2022;22(1):940. doi: 10.1186/s12885-022-10039-y.

[7] Cooks T, Theodorou SD, Paparouna E, et al. Immunohisto(cyto)chemistry: an old time classic tool driving modern oncological therapies. Histol Histopathol. 2019;34(4):335-352. doi: 10.14670/HH-18-069.

[8] Liu Y, Su Z, Tavana O, et al. Understanding the complexity of p53 in a new era of tumor suppression. Cancer Cell. 2024;42(6):946-967. doi: 10.1016/j.ccell.2024.04.009.

[9] Huang H, Chen F. Molecular and histological profiles and relevant imaging signatures of intrahepatic cholangiocarcinoma. J Clin Transl Hepatol. 2025;000(000):000-000. doi: 10.14218/JCTH.2024.00410.

[10] Khadiullina R, Mirgayazova R, Davletshin D, et al. Assessment of thermal stability of mutant p53 proteins via differential scanning fluorimetry. Life (Basel). 2022;13(1):31. doi: 10.3390/life13010031.

[11] Tomlinson JL, Li B, Yang J, et al. Syngeneic murine models with distinct immune microenvironments represent subsets of human intrahepatic cholangiocarcinoma. J Hepatol. 2024;80(6):892-903. doi: 10.1016/j.jhep.2024.02.008.

[12] Boldrin E, Piano MA, Bernaudo F, et al. p53/*TP53* status assessment in gastroesophageal adenocarcinoma. Cancers (Basel). 2023;15(10):2783. doi: 10.3390/cancers15102783.

[13] Liu Z, Luo C, Chen X, et al. Noninvasive prediction of perineural invasion in intrahepatic cholangiocarcinoma by clinicoradiological features and computed tomography radiomics based on interpretable machine learning: a multicenter cohort study. Int J Surg. 2024;110(2):1039-1051. doi: 10.1097/JS9.0000000000000881.

[14] Sheng R, Zhang Y, Wang H, et al. A multi-center diagnostic system for intrahepatic

mass-forming cholangiocarcinoma based on preoperative MRI and clinical features. Eur Radiol. 2024;34(1):548-559. doi: 10.1007/s00330-023-10002-w.

[15] Jin KP, Sheng RF, Yang C, et al. Combined arterial and delayed enhancement patterns of MRI assist in prognostic prediction for intrahepatic mass-forming cholangiocarcinoma (IMCC). Abdom Radiol (NY). 2022;47(2):640-650. doi: 10.1007/s00261-021-03292-5.

[16] Shahbazian H, Mirza-Aghazadeh-Attari M, Borhani A, et al. Multimodality imaging of hepatocellular carcinoma and intrahepatic cholangiocarcinoma. J Surg Oncol. 2023;128(4):519-530. doi: 10.1002/jso.27396.

[17] Yang Y, Fang S, Tao J, et al. Correlation of apparent diffusion coefficient with proliferation and apoptotic indexes in a murine model of fibrosarcoma: comparison of four methods for MRI region of interest positioning. J Magn Reson Imaging. 2023;57(5):1406-1413. doi: 10.1002/jmri.28371.

[18] Xing LH, Zhuo LY, Wang JN, et al. Values of MRI imaging presentations in the hepatobiliary phase, DWI and T2WI sequences in predicting pathological grades of intrahepatic mass-forming cholangiocarcinoma. Front Oncol. 2022;12:867702. doi: 10.3389/fonc.2022.867702.

[19] Ma C, Wang L, Song D, et al. Multimodal-based machine learning strategy for accurate and non-invasive prediction of intramedullary glioma grade and mutation status of molecular markers: a retrospective study. BMC Med. 2023;21(1):198. doi:

10.1186/s12916-023-02898-4.

[20] Shen L, Dai B, Dou S, et al. Estimation of *TP53* mutations for endometrial cancer based on diffusion-weighted imaging deep learning and radiomics features. BMC Cancer. 2025;25(1):45. doi: 10.1186/s12885-025-13424-5.

[21] Wang C, Wang C, Wang Q, et al. Preoperative MVI prediction in intrahepatic cholangiocarcinoma via deep learning analysis of intratumoral and peritumoral features on multi-sequence MRI. BMC Med Imaging. 2025;26(1):33. doi: 10.1186/s12880-025-02107-z.

[22] Choi SY, Kim YK, Min JH, et al. Added value of ancillary imaging features for differentiating scirrhous hepatocellular carcinoma from intrahepatic cholangiocarcinoma on gadoxetic acid-enhanced MR imaging. Eur Radiol. 2018;28(6):2549-2560. doi: 10.1007/s00330-017-5196-y.

[23] Lewis S, Besa C, Wagner M, et al. Prediction of the histopathologic findings of intrahepatic cholangiocarcinoma: qualitative and quantitative assessment of diffusion-weighted imaging. Eur Radiol. 2018;28(5):2047-2057. doi: 10.1007/s00330-017-5156-6.

[24] Greten TF, Schwabe R, Bardeesy N, et al. Immunology and immunotherapy of cholangiocarcinoma. Nat Rev Gastroenterol Hepatol. 2023;20(6):349-365. doi: 10.1038/s41575-022-00741-4.

[25] Dar FS, Abbas Z, Ahmed I, et al. National guidelines for the diagnosis and treatment of hilar cholangiocarcinoma. World J Gastroenterol. 2024;30(9):1018-1042. doi: 10.3748/wjg.v30.i9.1018.

[26] Chen RX, Liu SC, Kan XC, et al. CircUGP2 suppresses intrahepatic cholangiocarcinoma progression via p53 signaling through interacting with PURB to regulate ADGRB1 transcription and sponging miR-3191-5p. Adv Sci (Weinh). 2024;11(38):e2402329. doi: 10.1002/advs.202402329.

[27] Fiz F, Masci C, Costa G, et al. PET/CT-based radiomics of mass-forming intrahepatic cholangiocarcinoma improves prediction of pathology data and survival. Eur J Nucl Med Mol Imaging. 2022;49(10):3387-3400. doi: 10.1007/s00259-022-05765-1.

[28] Pan YJ, Wu SJ, Zeng Y, et al. Intra- and peri-tumoral radiomics based on dynamic contrast enhanced-MRI to identify lymph node metastasis and prognosis in intrahepatic cholangiocarcinoma. J Magn Reson Imaging. 2024;60(6):2669-2680. doi: 10.1002/jmri.29390.

[29] Xu L, Wan Y, Luo C, et al. Integrating intratumoral and peritumoral features to predict tumor recurrence in intrahepatic cholangiocarcinoma. Phys Med Biol. 2021;66(12):125001. doi: 10.1088/1361-6560/ac01f3.

[30] Huang Z, Mo S, Wu H, et al. Optimizing breast cancer diagnosis with photoacoustic imaging: an analysis of intratumoral and peritumoral radiomics. Photoacoustics.

2024;38:100606. doi: 10.1016/j.pacs.2024.100606.

[31] Xu Y, Ye F, Li L, et al. MRI-based radiomics nomogram for preoperatively differentiating intrahepatic mass-forming cholangiocarcinoma from resectable colorectal liver metastases. Acad Radiol. 2023;30(9):2010-2020. doi: 10.1016/j.acra.2023.04.030.

[32] Ji GW, Xu Q, Jiao CY, et al. Translating imaging traits of mass-forming intrahepatic cholangiocarcinoma into the clinic: from prognostic to therapeutic insights. JHEP Rep. 2023;5(10):100839. doi: 10.1016/j.jhepr.2023.100839.

[33] Liu N, Wu Y, Tao Y, et al. Differentiation of hepatocellular carcinoma from intrahepatic cholangiocarcinoma through MRI radiomics. Cancers (Basel). 2023;15(22):5373. doi: 10.3390/cancers15225373.

[34] Qian X, Zhou C, Wang F, et al. Development and validation of combined Ki67 status prediction model for intrahepatic cholangiocarcinoma based on clinicoradiological features and MRI radiomics. Radiol Med. 2023;128(3):274-288. doi: 10.1007/s11547-023-01597-7.

[35] Wang Y, Guan X, Ma S, et al. An MRI radiomics approach using invasion-based weak supervision for identifying and evaluating aggressive PitNETs. NPJ Digit Med. 2025;9(1):17. doi: 10.1038/s41746-025-02189-7.

Figure legends

Figure 1 Patient enrollment flowchart.

Figure 2 Receiver operating characteristic (ROC) curves of the seven machine learning models in the training cohort (Figure a) and the internal validation cohort (Figure b）

Figure 3 Receiver operating characteristic (ROC) curves of the radiomics models based on the T2WI sequence (a-b) and the DWI sequence (c-d) in the training cohort (a, c) and the internal validation cohort (b, d).

Figure 4 Receiver operating characteristic (ROC) curves of the Union Model, fuision Model, and Clinical Model in the training cohort (a), internal validation cohort (b), and external validation cohort (c).

Figure 5 Confusion matrix plots for the Fusion Model (a, d, g), Clinical Model (b, e, h), and the Union model (c, f, i) across the training cohort (a-c), internal validation cohort (d-f), and external validation cohort (g-i).

Figure 6 SHAP analysis of features for predicting p53-positive expression in the Union Model

Figure 7 (a) and (b) show the DWI and T2WI sequence images of a 65-year-old female patient with p53-negative expression; (c) and (d) show the DWI and T2WI sequence images of a 53-year-old male patient with p53-positive expression.

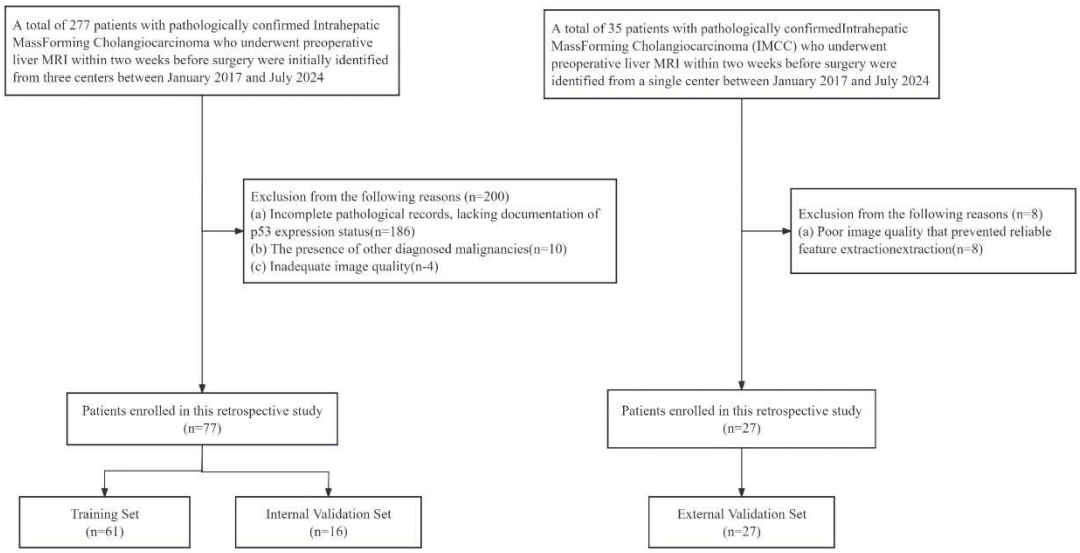


Figure 1

a. b.

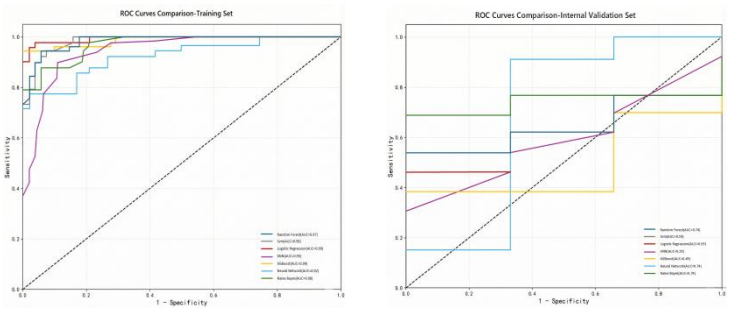


Figure 2

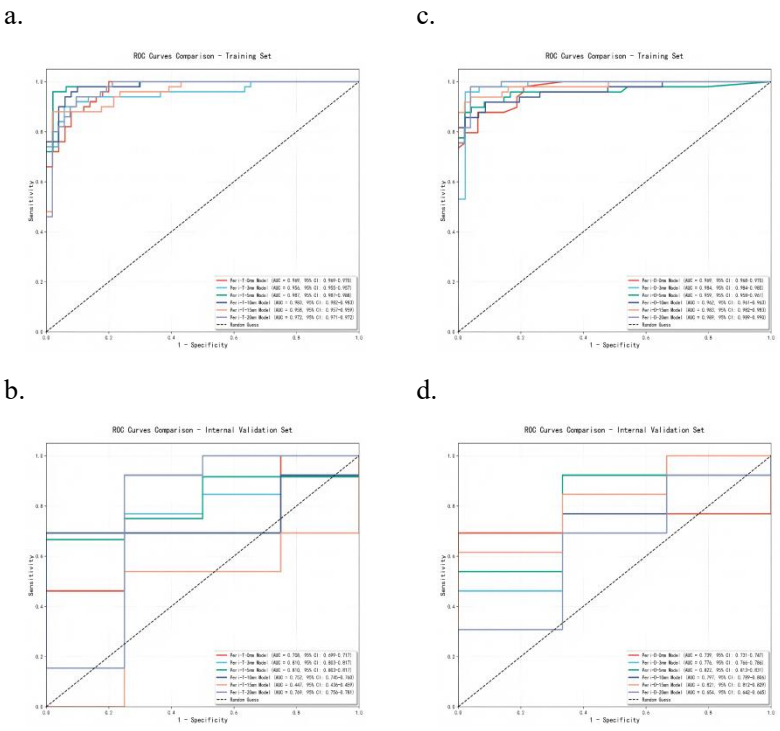


Figure 3

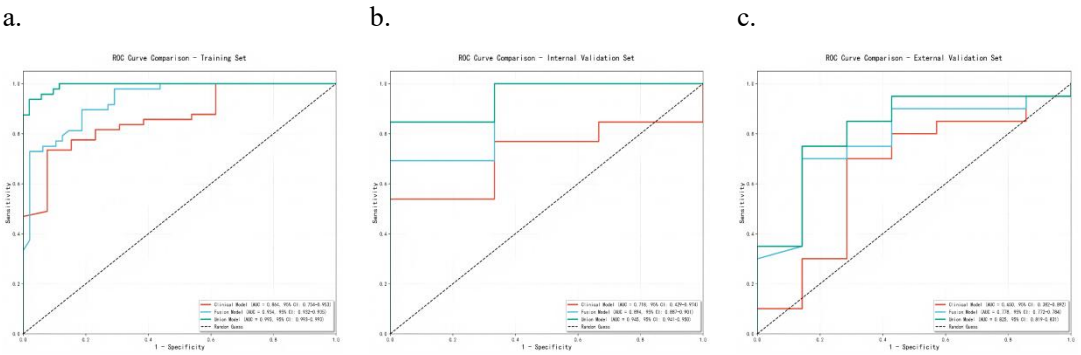
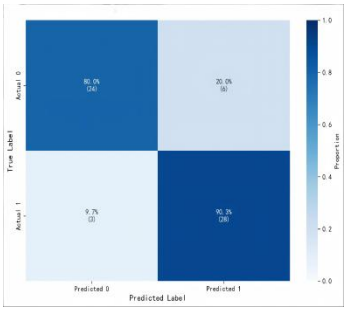
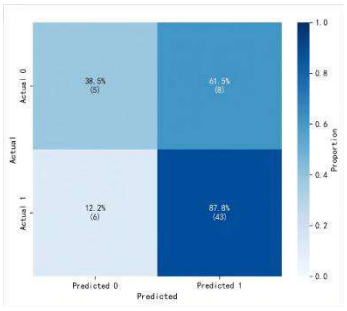


Figure 4

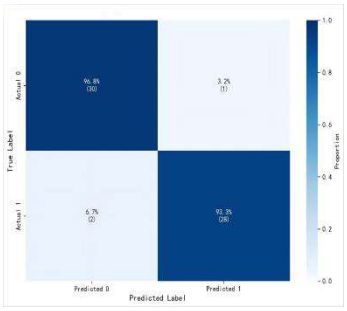
a.



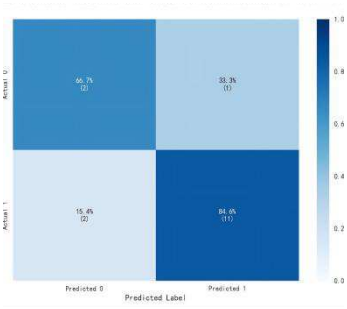
b.



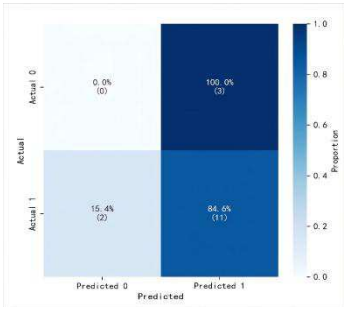
c.



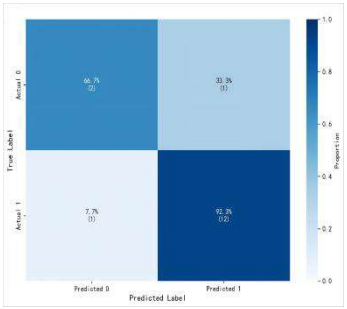
d.



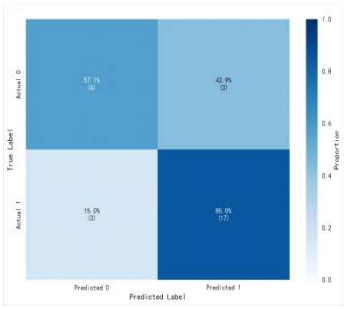
e.



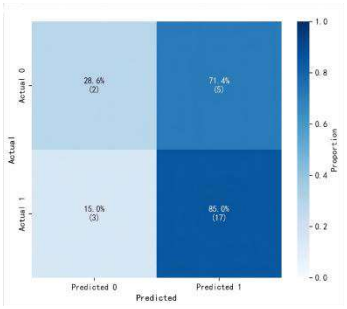
f.



g.



h.



i.

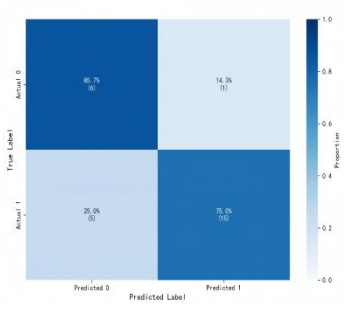


Figure 5

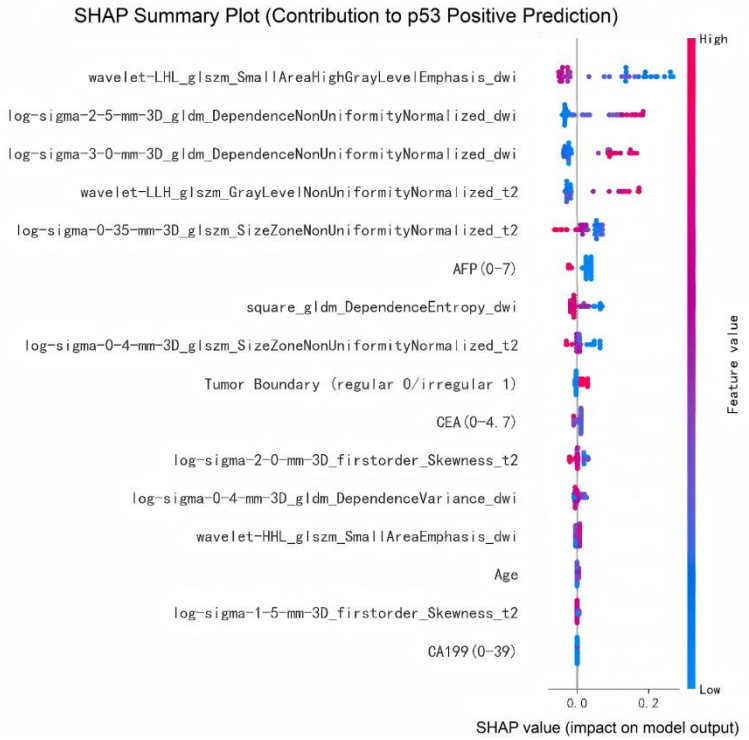
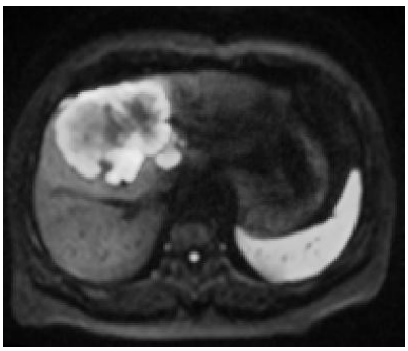


Figure 6

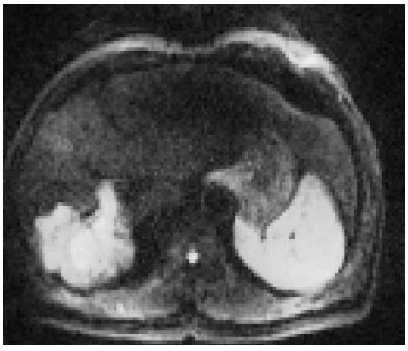
a.



b.



c.



d.



Figure 7

Table 1. Clinical and imaging characteristics of intrahepatic mass-forming cholangiocarcinoma (IMCC) patients in the training cohort, internal validation cohort, and external validation cohort

Characteristics	Training / Internal validation Cohort(*n*=77)		t/χ^2	p value	External validation Cohort (*n*=27)		t/χ^2	p value
	p53-(n=16)	p53+(n=61)			P53-(n=9)	P53+(n=18)		
Age(years)	61.4±11.4	58.6±11.1	0.900①	0.370	54.7±4.4	60.2±10.8	-1.450①	0.159
Gender(%)			0.003②	0.954			3.134②	3.134②
Female	6 (37.5)	20 (32.8)			2 (22.2)	12 (66.7)		
Male	10 (62.5)	41 (67.2)			7 (77.8)	6 (33.3)		
CA199(%)	157±333	219±933	-0.260①	0.795	336±395	193±317	1.020①	0.317
CEA(%)	5.0±6.2	8.5±42.3	-0.330①	0.743	77.8±207	5.5±7.0	1.510①	0.144
AFP(%)	76.9±224	365±2782	-0.410①	0.681	37.9±90.6	30.7±64.1	0.240①	0.812
CA125(%)	18.3±8.8	37.4±95.0	-0.800①	0.426	56.6±34.6	57.5±82.4	-0.030①	0.976
Lesion location(%)			2.898②	0.235			1.736②	0.420
left lobe	6 (37.5)	15 (24.6)			4 (44.4)	6 (33.3)		
right lobe	9 (56.3)	31 (50.8)			5 (55.6%)	9 (50.0)		
Both lobes involved	1 (6.3)	15 (24.6)			0 (0.0)	3 (16.7)		
Tumor morphology(%)			0.784②	0.376			0.555②	0.456
regular	5 (31.3)	29 (47.5)			4 (44.4)	4 (22.2)		
irregular	11 (68.8)	32 (52.5)			5 (55.6)	14 (77.8)		
T2WI tumor boundary(%)			1.243②	0.265			0.973②	0.324
well-defined	11 (68.8)	30 (49.2)			4 (44.4)	13 (72.2)		
poorly defined	5 (31.3)	31 (50.8)			5 (55.6)	5 (27.8)		
Peritumoral bile duct dilation(%)			—	1③			0.022②	0.882
non-presence	11 (68.8)	42 (68.9)			7 (77.8)	12 (66.7)		
presence	5 (31.3)	19 (31.1)			2 (22.2)	6 (33.3)		
Liver capsule retraction(%)			0.444②	0.505			0.464②	0.496
non-presence	13 (81.3)	42 (68.9)			3 (33.3)	10 (55.6)		
presence	3 (18.8)	19 (31.1)			6 (66.7)	8 (44.4)		
Intrahepatic bile duct stones(%)			—	1③			—	1③
non-presence	16 (100.0)	60 (98.4)			9 (100.0)	17 (94.4)		
presence	0 (0.0)	1 (1.6)			0 (0.0)	1 (5.6)		
Vascular involvement(%)			0.087②	0.768			—	1③
non-presence	12 (75.0)	41 (67.2)			5 (55.6)	10 (55.6)		
presence	4 (25.0)	20 (32.8)			4 (44.4)	8 (44.4)		
vascular penetration sign(%)			0.087②	0.768			1.181②	0.277
non-presence	12 (75.0)	41 (67.2)			5 (55.6)	15 (83.3)		
presence	4 (25.0)	20 (32.8)			4 (44.4)	3 (16.7)		
Suspicious lymph nodes(%)			—	1③			0.024②	0.877

non-presence	13 (81.3)	50 (82.0)			6 (66.7)	14 (77.8)		
presence	3 (18.8)	11 (18.0)			3 (33.3)	4 (22.2)		
T2 signal(%)			1.940②	0.746			2.550②	0.466
uniform high signal	4(25.0)	14(23.0)			5(55.6)	5(27.8)		
heterogeneous high signal	11(68.8)	35(57.4)			4(44.4)	11(61.1)		
peripheral high signal with central low signal	0	3(4.9)			0	1(5.6)		
isointense signal	1(6.3)	9(14.8)			0	1(5.6)		
DWI signal (%)			0.650②	0.724			3.240②	0.198
uniform high signal	3(18.8)	12(19.7)			5(55.6)	4(22.2)		
heterogeneous high signal	10(62.5)	32(52.5)			4(44.4)	13(72.2)		
peripheral high signal with central low signal	3(18.8)	17(27.9)			0	1(5.6)		

(Note: ① independent-samples *t*-test, ② chi-square test, and ③ Fisher's exact test. An independent-samples t-test was used for continuous variables conforming to normal distribution, and the chi-square test or Fisher's exact test was used for categorical variables.)

Table 2. Predictive performance of the twelve single-sequence radiomics models in the training and internal validation cohorts

Cohort	Models	AUC（95% CI）	Accuracy	Sensitivity	Specificity
Training	Peri-D-0mm	0.969(0.978,0.970)	0.877	0.777	0.978
	Peri-D-3mm	0.984（0.983,0.985）	0.893	0.817	0.976
	Peri-D-5mm	0.959（0.958,0.960）	0.804	0.612	1
	Peri-D-10mm	0.961（0.960,0.963）	0.842	0.693	1
	Peri-D-15mm	0.982（0.981,0.983）	0.879	0.755	1
	Peri-D-20mm	0.989（0.989,0.990）	0.869	0.755	0.980
	Peri-T-0mm	0.969(0.968,0.970)	0.851	0.722	0.980
	Peri-T-3mm	0.956(0.954,0.957)	0.706	0.398	1
	Peri-T-5mm	0.987(0.986,0.988)	0.804	0.619	1
	Peri-T-10mm	0.982(0.982,0.983)	0.82	0.640	1
	Peri-T-15mm	0.958(0.957,0.959)	0.811	0.638	0.979
	Peri-T-20mm	0.971(0.970,0.972)	0.843	0.722	0.980
Internal validation	Peri-D-0mm	0.739（0.731,0.747）	0.681	0.683	0.668
	Peri-D-3mm	0.775（0.765,0.785）	0.806	0.926	0.315
	Peri-D-5mm	0.821（0.812,0.831）	0.746	0.764	0.668
	Peri-D-10mm	0.797（0.788,0.806）	0.623	0.611	0.675
	Peri-D-15mm	0.820（0.812,0.829）	0.622	0.608	0.674
	Peri-D-20mm	0.653（0.641,0.665）	0.630	0.699	0.356
	Peri-T-0mm	0.707(0.698,0.716)	0.76	0.922	0.247
	Peri-T-3mm	0.809(0.803,0.816)	0.707	0.613	1
	Peri-T-5mm	0.809(0.802,0.817)	0.748	0.744	0.760
	Peri-T-10mm	0.752(0.744,0.960)	0.768	0.693	1
	Peri-T-15mm	0.447(0.435,0.459)	0.53	0.461	0.751
	Peri-T-20mm	0.768(0.956,0.981)	0.703	0.687	0.748

(Note: AUC: area under the curve; CI: confidence interval; DWI: diffusion-weighted imaging; Peri-D: radiomics model based on the DWI sequence; Peri-T: radiomics model based on the T2WI sequence)

Table 3. Predictive Performance of the Union Model, Fusion Model, and Clinical Model in the Training Cohort, Internal Validation Cohort, and External Validation Cohort

Cohort	Models	AUC（95% CI）	Accuracy	Sensitivity	Specificity
Training	Union model	0.992(0.992,0.993)	0.958	0.934	0.98
	Fusion model	0.933(0.932,0.935)	0.853	0.893	0.813
	Clinical model	0.864(0.754,0.953)	0.774	0.878	0.385
Internal validation	Union model	0.945(0.941,0.949)	0.868	0.919	0.660
	Fusion model	0.894(0.887,0.901)	0.808	0.844	0.660
	Clinical model	0.718(0.429,0.974)	0.688	0.846	0
External validation	Union model	0.825(0.819,0.831)	0.780	0.751	0.865
	Fusion model	0.777(0.771,0.784)	0.777	0.851	0.570
	Clinical model	0.650(0.382,0.892)	0.704	0.850	0.286

（Note: AUC: area under the curve; CI: confidence interval）

Supplementary Files

This is a list of supplementary files associated with this preprint. Click to download.

- Supplementarymaterial1.docx